

## VLA MAPPING OF THE CO(1–0) LINE IN SMM J14011+0252

CHELSEA E. SHARON, ANDREW J. BAKER

Department of Physics and Astronomy, Rutgers, the State University of New Jersey, Piscataway, NJ, 08854-8019

ANDREW I. HARRIS

Department of Astronomy, University of Maryland, College Park, MD 20742

AND

ALASDAIR P. THOMSON

Institute for Astronomy, University of Edinburgh, Blackford Hill, Edinburgh EH9 3HJ, UK

*ApJ Accepted 12/24/2012*

### ABSTRACT

We present high-resolution CO(1–0) observations of the lensed submillimeter galaxy (SMG) SMM J14011+0252 at  $z = 2.6$ . Comparison to the previously-detected CO(3–2) line gives an intensity ratio of  $r_{3,1} = 0.97 \pm 0.16$  in temperature units, larger than is typical for SMGs but within the range seen in the low- $z$  ultraluminous infrared galaxy population. Combining our new data with previous mid- $J$  CO observations, we perform a single-phase large velocity gradient (LVG) analysis to constrain the physical conditions of the molecular gas. Acceptable models have significant degeneracies between parameters, even when we rule out all models that produce optically thin emission, but we find that the bulk of the molecular gas has  $T_{\text{kin}} = 20\text{--}60$  K,  $n_{\text{H}_2} \sim 10^4\text{--}10^5$  cm<sup>-3</sup>, and  $N_{\text{CO}}/\Delta v = 10^{17.00 \pm 0.25}$  cm<sup>-2</sup> km<sup>-1</sup> s. For our best-fit models to self-consistently recover a typical CO-to-H<sub>2</sub> abundance and a plausible degree of virialization, the local velocity gradient in the molecular gas must be substantially larger than its galaxy-wide average. This conclusion is consistent with a scenario in which SMM J14011+0252 has a fairly face-on orientation and a molecular ISM composed of many unresolved clouds. Using previous H $\alpha$  observations, we find that SMM J14011+0252 has a spatially resolved star formation rate vs. molecular gas surface density relation inconsistent with those of “normal” local star-forming galaxies, even if we adopt a local “disk-like” CO-to-H<sub>2</sub> conversion factor as motivated by our LVG analysis. This discrepancy supports the inference of a star formation relation for high- $z$  starbursts distinct from the local relation that is not solely due to differing choices of gas mass conversion factor.

*Subject headings:* galaxies: high-redshift—galaxies: individual (SMM J14011+0252)—galaxies: ISM—galaxies: starburst—galaxies: star formation—ISM: molecules

### 1. INTRODUCTION

Since the discovery of a population of dusty, high-redshift submillimeter galaxies (SMGs), whose high star formation rates (SFRs) mean they contribute substantially to the cosmic infrared background (see review article by Blain et al. 2002), significant efforts have been made to characterize their star-forming molecular gas (e.g., Frayer et al. 1998, 1999; Neri et al. 2003; Greve et al. 2005; Tacconi et al. 2006, 2008). While many of these studies have used solely mid- $J$  CO lines (i.e., CO(3–2), CO(4–3), and CO(5–4)), recent expansions of the frequency coverage of radio telescopes into the Ka band have allowed observations of CO(1–0)—the best tracer of cold and low-density molecular gas—for SMGs whose redshifts fall near the  $z \sim 2\text{--}3$  peak of the distribution for radio-identified samples (Chapman et al. 2005). These build on observations of CO(1–0) for other  $z > 1$  populations in other bands (e.g., Papadopoulos et al. 2001; Carilli et al. 2002; Greve et al. 2003, 2004; Klamer et al. 2005; Hainline et al. 2006; Riechers et al. 2006; Dan-

nerbauer et al. 2009; Carilli et al. 2010; Aravena et al. 2010). The SMG studies have shown that the CO(3–2) to CO(1–0) line ratio favors a value of  $r_{3,1} \sim 0.6$  (in units of brightness temperature), indicating the presence of a multi-phase molecular ISM that includes a substantial cold gas reservoir (Swinbank et al. 2010; Harris et al. 2010; Ivison et al. 2011; Danielson et al. 2011). While similar line ratios have been observed in other types of high-redshift star-forming systems like Lyman break galaxies (Riechers et al. 2010) and BzK-selected galaxies (Dannerbauer et al. 2009; Aravena et al. 2010), and in low-redshift dusty galaxies (albeit with a much wider range of  $r_{3,1}$ ; e.g., Mauersberger et al. 1999; Yao et al. 2003), this result is in direct contrast to those for quasar host galaxies, whose near-unity value of  $r_{3,1}$  is consistent with single-phase molecular gas (Riechers et al. 2006, 2011a; see also  $r_{4,1} \gtrsim 1$  in Ivison et al. 2012).

While these CO(1–0) measurements have been essential for determining the *global* multi-phase nature of the molecular gas in SMGs, the lack of high-resolution mapping leaves some margin for error in interpreting line ratios. In order to be confident in assessing physical conditions in the gas, we need to know that the CO lines are being emitted from the same localized regions.

Given the clumpy structure observed in SMGs (e.g., Tacconi et al. 2008; Swinbank et al. 2010), and the role major mergers are likely playing in the star formation bursts of (at least) some of these systems (e.g., Conselice et al. 2003; Narayanan et al. 2010; Engel et al. 2010; Davé et al. 2010), it is not safe to assume a homogeneous distribution of gas conditions within every galaxy (e.g., Mao et al. 2000; Zhu et al. 2003). In addition, since many of the well-studied SMGs are gravitationally lensed, it is possible that differential lensing (the variation in magnification factor across a spatially extended source) could be affecting the observed line ratios (e.g., Blain 1999; Serjeant 2012). Indirect evidence for the spatial variation of excitation in SMGs has been seen in the more extended distribution of CO(1–0) relative to radio continuum emission (from the synchrotron radiation from supernova remnants, which trace more actively star-forming and thus higher-excitation gas; Ivison et al. 2011). The larger spatial extent of SMGs’ cold gas reservoirs is also bolstered by the larger line widths of CO(1–0) vs. CO(3–2) (Ivison et al. 2011; Thomson et al. 2012).

The high-resolution CO observations necessary for evaluating spatial variation of CO excitation also enable *spatially resolved* comparisons between the Schmidt-Kennicutt relations (Schmidt 1959; Kennicutt 1998) seen at low and high redshifts. Determining galaxies’ gas mass surface densities from CO surface brightness requires the assumption of a CO-to-H<sub>2</sub> conversion factor. Observations of high, and sometimes unphysical, gas mass fractions in low-*z* IR-bright starbursts and some disk galaxy centers (e.g., Scoville et al. 1991; Garcia-Burillo et al. 1993; Downes et al. 1993; Solomon et al. 1997; Scoville et al. 1997; Oka et al. 1998; Hinz & Rieke 2006; Meier et al. 2010) imply a range of  $\alpha_{\text{CO}}$ , leading to the adoption of a “disk” value ( $\alpha_{\text{CO}} = 4.6 M_{\odot} (\text{K km s}^{-1} \text{pc}^2)^{-1}$ ; Solomon & Barrett 1991) for normal star-forming galaxies and a “starburst” value ( $\alpha_{\text{CO}} = 0.8 M_{\odot} (\text{K km s}^{-1} \text{pc}^2)^{-1}$ ; Downes & Solomon 1998) for mergers and other high surface density environments. Some effort has been made to find a suitable continuous form of  $\alpha_{\text{CO}}$  (e.g., Glover & Mac Low 2011; Narayanan et al. 2012) that also matches observed trends in metallicity (e.g., Wilson 1995; Arimoto et al. 1996; Israel 1997; Leroy et al. 2006; Bolatto et al. 2008; Genzel et al. 2012). Which value (or values) of  $\alpha_{\text{CO}}$  is appropriate for high-redshift galaxies is debated (e.g., Tacconi et al. 2008), and the apparent bimodality in the high-*z* Schmidt-Kennicutt relation (where SMGs fall along the low-*z* starburst track, and more “normal” high-*z* galaxies extend the low-*z* disk galaxy track to higher masses and star formation rates; e.g., Daddi et al. 2010; Genzel et al. 2010; cf. Ivison et al. 2011) may be caused in part by the choice of  $\alpha_{\text{CO}}$ . Comparisons between the Schmidt-Kennicutt relations at high and low redshifts may also be affected by the differences in the CO lines observed (Narayanan et al. 2011), as the molecular gas at low redshift is measured via the CO(1–0) line, while the molecular gas at high redshift has typically been measured via mid-*J* CO lines. While galaxy-wide measurements of the star formation rate and molecular gas mass are typical for high-*z* systems, evaluation of the true surface density version of the Schmidt-Kennicutt relation

(e.g., Kennicutt et al. 2007; Bigiel et al. 2008; Wei et al. 2010) requires spatially resolved maps of CO lines and star formation tracers.

In order to explore the spatial variation of CO line ratios and the Schmidt-Kennicutt relation for high-*z* starbursts, we have obtained high-resolution Karl G. Jansky Very Large Array (VLA) mapping of the CO(1–0) line in SMM J14011+0252 (J14011 hereafter), which we compare to previous mid-*J* and rest-frame mid-IR observations. J14011 ( $z_{\text{opt}} = 2.55$ ; Barger et al. 1999) was discovered as part of the SCUBA Lens Survey (Smail et al. 1998, 2002); it consists of two optical/near-IR components in the source plane (J1 and J2) that are weakly gravitationally lensed by the cluster A1835 ( $z = 0.25$ ) and one of its members (J1c; Motohara et al. 2005), with a median magnification factor of  $\mu \sim 3.5 \pm 0.5$  (Smail et al. 2005). Since its discovery, J14011 has been followed up extensively with optical and near-IR observations (Barger et al. 1999; Ivison et al. 2000, 2001; Tecza et al. 2004; Frayer et al. 2004; Swinbank et al. 2004; Motohara et al. 2005; Nesvadba et al. 2007), and it was only the second SMG to be successfully detected in any CO transition (CO(3–2); Frayer et al. 1999). Further CO(3–2) observations were made by Ivison et al. (2001), as were CO(3–2) and CO(7–6) observations by Downes & Solomon (2003). Strong upper limits on its X-ray flux (Ivison et al. 2000; Fabian et al. 2000; Rigby et al. 2008) and ratios of the 7.7  $\mu\text{m}$  polycyclic aromatic hydrocarbon (PAH) feature to mid-infrared flux (Rigby et al. 2008) indicate that J14011 is a pure starburst, lacking a significant contribution to its dust luminosity from an active galactic nucleus (AGN). It is similar in its far-infrared luminosity ( $L_{\text{FIR}} \sim 4 \times 10^{12} L_{\odot}$ ; Smail et al. 2005) and its clumpy morphology within and between optical/near-IR components (Ivison et al. 2000; Tecza et al. 2004; Swinbank et al. 2004) to low-redshift ultra/luminous infrared galaxies (U/LIRGs) such as Arp 220 (Frayer et al. 1999; Ivison et al. 2000; Downes & Solomon 2003; Motohara et al. 2005; Nesvadba et al. 2007; Rigby et al. 2008). Initial single-dish observations of the CO(1–0) line indicated  $r_{3,1} = 0.76 \pm 0.12$  (Harris et al. 2010), similar to the values seen for other SMGs.

We assume the WMAP7+BAO+ $H_0$  mean  $\Lambda$ CDM cosmology throughout this paper, with  $\Omega_{\Lambda} = 0.725$  and  $H_0 = 70.2 \text{ km s}^{-1} \text{ Mpc}^{-1}$  (Komatsu et al. 2011).

## 2. OBSERVATIONS

We observed J14011 ( $\alpha(\text{J2000}) = 14^{\text{h}}01^{\text{m}}4.^{\text{s}}93$ ,  $\delta(\text{J2000}) = +02^{\circ}52'24.1''$ ; CO(3–2) position from Downes & Solomon 2003) at the VLA on 2010 October 1 and 3 in the DnC configuration (maximum baseline 1.868 km) and 2011 January 22, 25, and 28–31 in the CnB configuration (maximum baseline 6.903 km). During the DnC observations, 23 antennas were functioning and equipped with Ka-band receivers, and the weather conditions were mixed ( $< 70\%$  sky coverage by cumuli-form clouds). During the CnB observations, 26 Ka-band-equipped antennas were available, and the weather conditions were excellent. We observed with the Wideband Interferometric Digital Architecture (WIDAR) correlator in the “Open Shared Risk Observing (OSRO) Full Polarization” mode using the lowest available spectral resolution (64 channels  $\times$  2 MHz resolution). The intermediate frequency (IF) channel pairs A/C and B/D were tuned

to overlap by ten channels, creating a full bandwidth of 236 MHz centered at 32.3703 GHz (chosen to keep the line away from IF pair edges). At the beginning of each track we observed 3C286 as a flux calibrator, adopting  $S_\nu = 1.9455$  Jy as the Common Astronomy Software Applications (CASA) package’s default “Perley-Butler 2010” flux density<sup>1</sup>. Phase and amplitude fluctuations were tracked by alternating between the source and a nearby quasar, J1354–0206, with a cycle time of 6 minutes; this quasar was also used for passband calibration. A total of 18.7 hours was spent on source.

Calibration and mapping were carried out in CASA<sup>1</sup>. After the tracks had been corrected for Doppler shifts relative to the local kinematic (radio) standard of rest using the CASA routine `cvel`, the original channels were smoothed by a factor of two, resulting in 4 MHz ( $37 \text{ km s}^{-1}$  rest frame) spectral resolution. The naturally weighted channel maps have a synthesized beam of  $0.''68 \times 0.''52$  at position angle 119.02 degrees and an average RMS noise of  $53.2 \mu\text{Jy beam}^{-1}$ . Analysis of the resulting data cube was performed using a custom set of IDL scripts.

### 3. RESULTS

Our spectrum (Fig. 1) successfully detects the CO(1–0) line at the  $8\sigma$  level. A Gaussian fit to our line profile gives a peak flux density of  $2.08 \pm 0.22$  mJy and a FWHM of  $151 \pm 19 \text{ km s}^{-1}$ . The FWHM is consistent with the CO(7–6) line width of  $170 \pm 30 \text{ km s}^{-1}$ , and marginally narrower than the CO(3–2) line width of  $190 \pm 11 \text{ km s}^{-1}$  from Downes & Solomon (2003). The integrated CO(1–0) line flux (using the seven channels around the line peak) is  $0.32 \pm 0.03 (\pm 0.03)$  Jy  $\text{km s}^{-1}$ , where the latter 10% uncertainty is associated with the flux calibration. While our measured integrated line flux appears to be lower than the  $\sim 0.40 \pm 0.05$  Jy  $\text{km s}^{-1}$  of Harris et al. (2010), the two values are consistent within their  $1\sigma$  errors. The slight discrepancy is likely because the Zpectrometer-measured value is from a Gaussian fit in which the line width is only an upper limit (the narrow line was marginally spectrally resolved by the Zpectrometer). Convolution of the VLA spectrum with the 20 MHz FWHM  $\text{sinc}(x)$  response function of the Zpectrometer reproduces the Gaussian fit integrated line flux given in Harris et al. (2010), indicating that our measurements are in good agreement when we account for spectral resolution differences. Using the Milky Way conversion factor  $\alpha_{\text{CO}} = 4.6 M_\odot (\text{K km s}^{-1} \text{pc}^2)^{-1}$  (Solomon & Barrett 1991) suggested by our LVG analysis (Section 4.1) and correcting for lensing magnification and helium, the molecular gas mass is  $(1.9 \pm 0.3) \times 10^{11} M_\odot$ . The redshift as determined by our CO(1–0) measurement is  $z = 2.5653 \pm 0.0001$ , which is consistent with the previous optical (e.g., Barger et al. 1999; Ivison et al. 2000) and CO (e.g., Downes & Solomon 2003; Harris et al. 2010) redshifts.

The integrated intensity map (Fig. 2) shows that the CO(1–0) emission is spatially extended in a northeast/southwest direction, parallel to the lensing shear (Smail et al. 2005), and contains two peaks embedded within more extended emission, similar to those seen

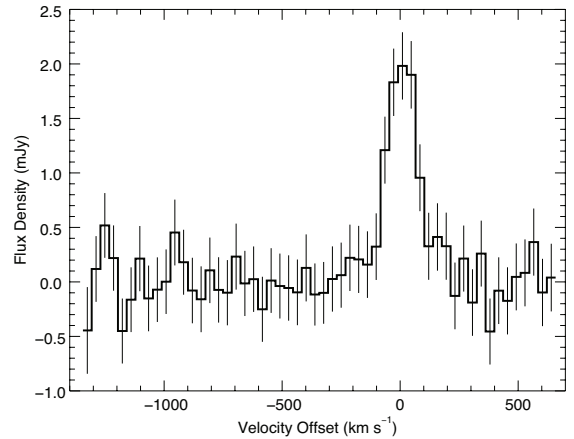


FIG. 1.—  $37 \text{ km s}^{-1}$  resolution VLA spectrum plotted relative to the  $z = 2.5652$  CO(1–0) systemic redshift from the GBT/Zpectrometer observations (Harris et al. 2010). Vertical lines indicate statistical uncertainties.

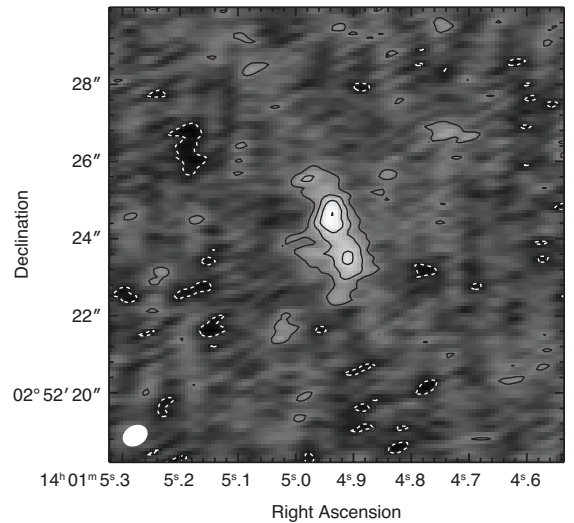


FIG. 2.— Integrated CO(1–0) intensity map. Contours are multiples of  $\pm 2\sigma$  ( $\sigma = 0.16 \text{ mJy beam}^{-1}$ ), where negative contours are dotted; synthesized beam is shown at lower left.

in  $\text{H}\alpha$  (Tecza et al. 2004). The center of the CO(1–0) line emission is consistent with the peak positions of the CO(3–2) and CO(7–6) lines previously detected by Downes & Solomon (2003) (Fig. 3), with  $\sigma_{1-0} = 0.''05$  based on an elliptical Gaussian fit in the image plane and the intrinsic uncertainty of the phase calibrator position. The Gaussian fit gives a major axis FWHM of  $2.''6 \pm 0.''1$  at position angle  $18.7 \pm 1.3$  degrees and a minor axis FWHM of  $0.''8 \pm 0.''1$  when accounting for the beam size. As J14011 is lensed, these dimensions do not easily translate into rest-frame physical dimensions. While the line FWHM is quite narrow, the CO(1–0) emission does show a velocity gradient. In Fig. 4, we plot overlaid channel maps of the red and blue halves of the central  $200 \text{ km s}^{-1}$  of CO(1–0) line as well as the same velocity ranges for the  $\text{H}\alpha$  integral field data presented in Tecza et al. (2004). The red and blue halves of both lines are slightly offset in similar directions, with the two peaks in the integrated line maps apparently dominated by emission at different velocities. In Fig. 4, we also show a CO(1–0) position-velocity diagram for J14011 for a po-

<sup>1</sup> <http://casa.nrao.edu>

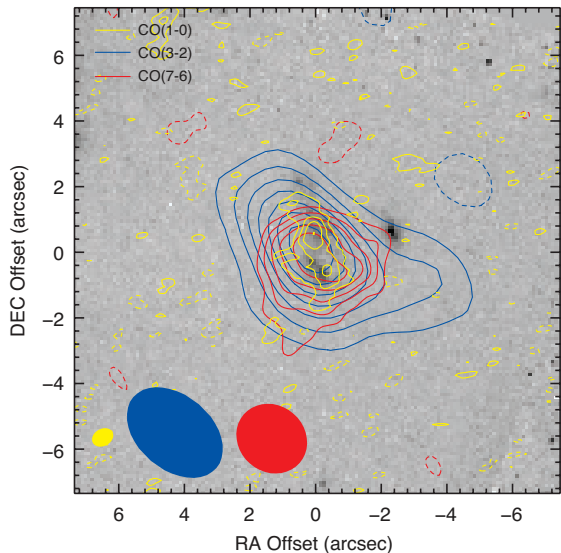


FIG. 3.— Overlaid contours of all published CO maps of J14011 and the Aguirre et al. (2012) *HST* F160W image (with the foreground interloper, J1c, removed), centered at  $\alpha(\text{J2000}) = 14^{\text{h}}01^{\text{m}}04.^{\text{s}}93$  and  $\delta(\text{J2000}) = +02^{\circ}52'24.''1$ . The CO(1–0), CO(3–2), and CO(7–6) maps are in yellow, blue, and red respectively; the synthesized beam for each map is shown by the filled ellipse of the corresponding color in the lower left corner. The CO(1–0) line contours are as described in Fig. 2. The CO(3–2) and CO(7–6) observations are taken from Downes & Solomon (2003). The CO(3–2) contours are multiples of  $\pm 2\sigma$ , where  $\sigma = 0.41 \text{ mJy beam}^{-1}$ . The CO(7–6) contours are in steps of  $\pm 1\sigma$ , starting at  $\pm 2\sigma$ , where  $\sigma = 1.3 \text{ mJy beam}^{-1}$ .

sition angle of  $75 \pm 5$  degrees that maximizes the velocity gradient.

We do not detect any significant continuum emission from J14011 in the (rest-frame) 2.6 mm continuum map produced from the line-free channels. We estimate a  $3\sigma$  upper limit for the continuum emission of  $26.7 \mu\text{Jy}$  for a point-like source, or  $157 \mu\text{Jy}$  when scaled to the dimensions of the CO(1–0) emission.

In order to compare the CO(1–0) emission to existing optical and infrared data, we have taken care in aligning images. Based on the source sizes and structures in the two sets of maps in Fig. 4, and the fact that  $\text{H}\alpha$  emission from HII regions is expected to follow molecular gas at this linear resolution, we can use the positions of the northern and southern peaks to better align the datasets. The average offset between the peaks was applied as a shift to align the SINFONI  $\text{H}\alpha$  data cube with the radio observations. The measured offset is  $0.''82$ , which corresponds to roughly  $\lesssim 2\times$  the SINFONI point spread function (the astrometric uncertainty of the CO(1–0) map is  $\sim 0.''09$ , including both statistical uncertainty and uncertainty due to the phase calibrator position). Based on this alignment, we use the continuum emission from the line-free channels of the SINFONI data-cube (at  $\sim 2.2 \mu\text{m}$ ) to extend the alignment to the *HST*/NICMOS F160W data of Aguirre et al. (2012). As we expect the continuum emission at both wavelengths to come from the same physical regions in the source, we use the continuum from the foreground interloper (J1c) and the UV-bright companion galaxy (J2) to determine the shift to apply to the *HST* image to align it with the  $\text{H}\alpha$  and thus CO(1–0) maps (Fig. 3). We measure an offset of  $0.''49$  between the F160W and  $2.2 \mu\text{m}$  maps, making the offset

between the CO(1–0) and *HST* maps  $< 0.''5$ .

## 4. ANALYSIS

### 4.1. LVG modeling

J14011 has integrated brightness temperature ratios  $r_{3,1} = 0.97 \pm 0.16$  and  $r_{7,1} = 0.20 \pm 0.04$ . Comparisons between the higher- $J$  and CO(1–0) emission (convolved to the resolutions of the higher- $J$  maps) do not show evidence for spatial variation of CO excitation. This value of  $r_{3,1}$  is larger than the typical  $r_{3,1} \sim 0.6$  for SMGs and more similar to the  $r_{3,1} \sim 1$  seen in high- $z$  quasar host galaxies. The strong upper limits on X-ray emission and observations of mid-IR PAH features indicate that J14011 likely does not contain an AGN of sufficient strength to influence the global gas conditions, making its near-unity  $r_{3,1}$  unusual for its class. However, among low- $z$  U/LIRGs (which also have an average  $r_{3,1} \sim 0.6$ ), there are a small number of starbursts that globally or locally have  $r_{3,1} \sim 1$  but lack AGN, such as NGC 3690 (Iono et al. 2009), UGC 8739 (Yao et al. 2003), the inner region of NGC 253 (e.g., Bayet et al. 2004), and the northeast lobe of M82 (e.g., Ward et al. 2003). While the high  $r_{3,1}$  of J14011 is rare for a pure starburst, it is not unique. Yao et al. (2003) propose that high CO excitation in U/LIRGs can be caused by a very high concentration of star formation, consistent with the finding of Iono et al. (2009) that the peak central  $r_{3,1}$  is greater than or equal to the global  $r_{3,1}$  in spatially resolved maps. If the duration of highly concentrated star formation (such that the global and “peak” CO excitation are identical) is short-lived, then it is sensible that only a small number of pure-starburst SMGs (or local U/LIRGs) will exhibit high  $r_{3,1}$ . Gas distributions that are compact relative to heating sources may be the trait that such systems share with quasar host galaxies.

In order to investigate the physical conditions of the gas that produces these ratios, we have undertaken an excitation analysis using a Large Velocity Gradient (LVG) model. The details of the LVG modeling and analysis are described in Sharon et al. (in prep.). In short, the model follows the method of Ward (2002), assumes a spherical cloud geometry, and is modified to include the effects of the cosmic microwave background (CMB). With observed CO transitions equal in number to the model parameters (kinetic temperature,  $\text{H}_2$  density, and CO column density per unity velocity gradient) and substantial degeneracies in the measured line ratios, we expect significant degeneracies between the allowed model parameters. We therefore use both a minimum  $\chi^2$  and a Bayesian analysis (the latter better capturing our uncertainties; Ward et al. 2003) to determine which model parameters best reproduce our measured line ratios. For the Bayesian analysis, we have applied logarithmic priors to the LVG model parameters to compensate for the large logarithmically-sampled parameter space, as opposed to the usual agnostic prior equal to unity.

The parameters of the minimum  $\chi^2$  model are  $T = 136 \text{ K}$ ,  $n_{\text{H}_2} = 10^{3.2} \text{ cm}^{-3}$ , and  $N_{\text{CO}}/\Delta v = 10^{17.25} \text{ cm}^{-2} \text{ km}^{-1} \text{ s}$ . However, there are significant degeneracies in all three parameters. For example, the Bayesian maximum probability model favors the opposite extreme in temperature-density parameter space:  $T = 24 \text{ K}$ ,  $n_{\text{H}_2} = 10^{5.6} \text{ cm}^{-3}$ , and  $N_{\text{CO}}/\Delta v =$

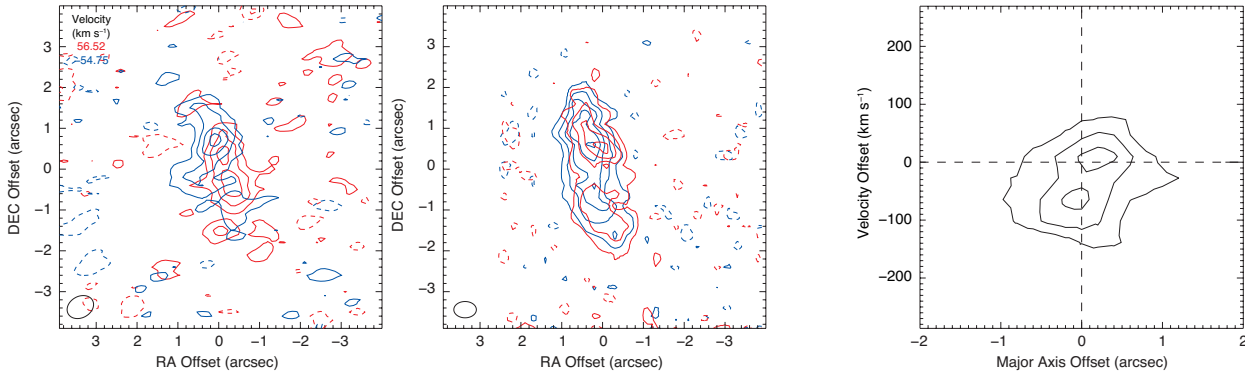


FIG. 4.— Left/Center: Overlaid contours of two 10 MHz ( $\sim 110 \text{ km s}^{-1}$ ) channels centered at  $56.52 \text{ km s}^{-1}$  (red lines) and  $-54.75 \text{ km s}^{-1}$  (blue lines) for the CO(1–0) line (left) and the H $\alpha$  line (center). Contours are multiples of  $\pm 2\sigma$  ( $\sigma_{1-0} = 0.17 \text{ mJy beam}^{-1}$ ;  $\sigma_{\text{H}\alpha} = 1.18 \times 10^{-18} \text{ W } \mu\text{m}^{-1} \text{ m}^{-2}$ ), where negative contours are dotted; synthesized beam/point spread function is shown at lower left. Right: Position-velocity diagram of the integrated line where the major axis (along the velocity gradient) is at a position angle of 75 degrees that maximizes the velocity gradient. Contours are multiples of  $1.75 \text{ mJy beam}^{-1}$ .

$10^{16.75} \text{ cm}^{-2} \text{ km}^{-1} \text{ s}$ . Similarly well-fitting models are produced for  $20 \text{ K} \lesssim T \lesssim 150 \text{ K}$  at comparable CO columns per velocity gradient ( $10^{17 \pm 0.25} \text{ cm}^{-2} \text{ km}^{-1} \text{ s}$ ), where lower temperature models favor higher H $_2$  densities ( $\sim 10^5 \text{ cm}^{-3}$ ) and higher temperature models favor lower H $_2$  densities ( $\sim 10^3 \text{ cm}^{-3}$ ). The optical depths produced by these two models are very different from one another. The minimum  $\chi^2$  model produces optically thick emission for the CO(3–2) and CO(7–6) transitions ( $\tau_{3-2} = 13.4$ ,  $\tau_{7-6} = 11.4$ ), and optically thin emission for the CO(1–0) transition ( $\tau_{1-0} = 0.7$ ). The cooler and more dense maximum probability model has the optical depths of the CO(1–0) and CO(7–6) lines reversed with  $\tau_{1-0} = 2.0$ ,  $\tau_{3-2} = 11.8$ , and  $\tau_{7-6} = 0.7$ . We also consider a restricted parameter space for the LVG models in which *all* of the measured lines must be produced by optically thick emission. The minimum  $\chi^2$  model with  $\tau_{J_{\text{upper}} \leq 7} > 1$  has a significantly lower temperature,  $T = 60 \text{ K}$ ,  $n_{\text{H}_2} = 10^{3.7} \text{ cm}^{-3}$ , and  $N_{\text{CO}}/\Delta v = 10^{17.25} \text{ cm}^{-2} \text{ km}^{-1} \text{ s}$ , while the maximum probability model only slightly increases in temperature (relative to the previous maximum probability model), with  $T = 28 \text{ K}$ ,  $n_{\text{H}_2} = 10^{5.0} \text{ cm}^{-3}$ , and  $N_{\text{CO}}/\Delta v = 10^{16.75} \text{ cm}^{-2} \text{ km}^{-1} \text{ s}$ . In these models, the optical depths of the CO(1–0) and CO(3–2) emission are comparable ( $\tau_{1-0} \approx 1.5$ ,  $\tau_{3-2} \sim 10\text{--}15$ ), but the CO(7–6) line is only just optically thick in the colder model, while in the warmer model the optical depth is a factor of  $\sim 10$  larger. The CO spectral line energy distributions (SLEDs) for these four models are shown in Fig. 5.

Our cooler and optically thick models favor kinetic temperatures comparable to the dust temperature,  $T_{\text{dust}} = 42 \text{ K}$  (Wu et al. 2009), and are in line with the results of other LVG analyses of SMGs (e.g., Weiß et al. 2007; Carilli et al. 2010; Riechers et al. 2010; Danielson et al. 2011; Riechers et al. 2011b). Observations of different molecular or atomic species can be useful for breaking temperature degeneracies in CO LVG models. Walter et al. (2011) make an independent estimate of the kinetic temperature in J14011 using their C I( $^3P_2 \rightarrow ^3P_1$ ) line measurement in conjunction with the previously-measured C I( $^3P_1 \rightarrow ^3P_0$ ) line (Weiß et al. 2005), deriving  $T_{\text{C I}} = 32.4 \pm 5.2 \text{ K}$ . At fixed  $T_{\text{kin}} = T_{\text{C I}}$ , the minimum  $\chi^2$  model (which is indistinguishable from the maximum probability model due to similar probabil-

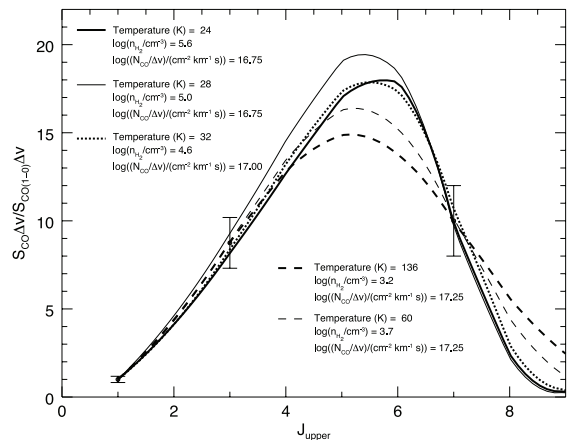


FIG. 5.— Measured line ratios (points; in flux units) and CO SLEDs for the maximum probability model (thick solid line), maximum probability model requiring  $\tau > 1$  (thin solid line), minimum  $\chi^2$  model (thick dashed line), minimum  $\chi^2$  model with  $\tau > 1$  (thin dashed line), and the maximum probability/minimum  $\chi^2$  model at fixed  $T_{\text{C I}}$  (thick dotted line). The LVG model parameters that produce these SLEDs are as labeled.

ity and  $\chi^2$  distributions in the  $n_{\text{H}_2}$ – $N_{\text{CO}}/\Delta v$  plane) has  $n_{\text{H}_2} = 10^{4.6} \text{ cm}^{-3}$  and  $N_{\text{CO}}/\Delta v = 10^{17.00} \text{ cm}^{-2} \text{ km}^{-1} \text{ s}$  (Fig. 5) and produces optically thick emission for all three transitions ( $\tau_{1-0} = 2.1$ ,  $\tau_{3-2} = 16.0$ ,  $\tau_{7-6} = 2.7$ ). While a prior LVG analysis performed by Bayet et al. (2009) preferred higher temperatures ( $T = 205 \text{ K}$ ) and lower densities ( $n_{\text{H}_2} = 10^{1.4} \text{ cm}^{-3}$ ) than any of our well-fitting models, due to the different goals of their work (predicting line strengths for a statistical sample rather than accurate determination of individual galaxy properties), given their use of only the CO(3–2) and CO(7–6) line measurements and our consistency with other estimates of the gas temperature, we view our results as more robust.

Besides the degeneracies between the best-fit models noted above, it is worth considering what degeneracies exist *within* each model (e.g., degeneracies between  $n_{\text{H}_2}$  and  $N_{\text{CO}}/\Delta v$  for a specific choice of temperature, or between  $T_{\text{kin}}$  and  $n_{\text{H}_2}$  for a specific value of  $N_{\text{CO}}/\Delta v$ ). In Fig. 6 we have plotted curves of constant probability (or  $\chi^2$ ) on the temperature-density plane for the best-fit values of  $N_{\text{CO}}/\Delta v$ . For a specific value of  $N_{\text{CO}}/\Delta v$ , there is generally an “L”-shaped region with nearly constant

probability/ $\chi^2$  that will reasonably reproduce a given CO line ratio. With multiple line ratios, the locus where the two “L”-shaped regions overlap produces the best-fit models. For multiple line ratios, these “L”-shaped regions overlap more for emission lines with similar optical depth ratios. The  $\tau > 1$  regions are marked with dashed lines in Fig. 6 and are also “L”-shaped. As optical depth is proportional to  $N_{\text{CO}}/\Delta v$ , larger regions satisfy the  $\tau > 1$  criterion for larger values of  $N_{\text{CO}}/\Delta v$ .

For a specific temperature, there are also degeneracies between the  $\text{H}_2$  density and CO column density per velocity gradient. In Fig. 7 we have plotted curves of constant  $\chi^2$  in the  $n_{\text{H}_2}$ - $N_{\text{CO}}/\Delta v$  plane for the optically thick model temperatures that give highest probability and minimum  $\chi^2$  (in this plane, the probability and  $\chi^2$  contours have the same shape, but are scaled differently since the probability is  $\propto e^{-\chi^2}$ ). While slightly shifted between the panels for the two temperatures, there is a clear linear valley with low  $\chi^2$ . This region corresponds to  $N_{\text{CO}}/\Delta v \propto n_{\text{H}_2}^{-1}$ , and it exists for all  $T_{\text{kin}} > 30\text{K}$  models (for  $T < 30\text{K}$ , the valley of low  $\chi^2$  values asymptotes to a single value of  $N_{\text{CO}}/\Delta v$  for higher  $\text{H}_2$  densities). This linear feature corresponds to a constant optical depth ratio for the emission lines that best reproduce the measured line ratios.

With these substantial degeneracies it is worth considering priors in addition to optical depth that might limit the allowed parameter ranges for the LVG models. Since the most dense molecular gas in the Galaxy is found in star-forming virialized clouds, we can consider placing limits on the density by considering the degree of virialization as parameterized by

$$K_{\text{vir}} \sim 1.54 \frac{[\text{CO}/\text{H}_2]}{\sqrt{a}\Lambda_{\text{CO}}} \left[ \frac{\langle n_{\text{H}_2} \rangle}{10^3 \text{ cm}^{-3}} \right]^{-1/2} \quad (1)$$

where  $\Lambda_{\text{CO}}$  is the CO abundance per unit velocity gradient and  $a \sim 1$ –2.5 is a constant that depends on the cloud geometry (e.g., Goldsmith 2001; Greve et al. 2009). In this parameterization,  $[\text{CO}/\text{H}_2] \Lambda_{\text{CO}}^{-1}$  is the velocity gradient in the molecular gas, and  $K_{\text{vir}} \ll 1$  is dynamically unobtainable. For J14011, the velocity gradient could be a value determined by global parameters (given by the  $\sim 150 \text{ km s}^{-1}$  CO(1–0) FWHM and approximate de-lensed optical source size of  $\sim 10 \text{ kpc}$  from Smail et al. (2005)) if the line luminosity is tracing the total gravitational potential of the galaxy (e.g., Downes et al. 1993), or a different value if the molecular gas is in individual star-forming clouds. For the global velocity gradient, requiring that  $K_{\text{vir}} > 0.1$  means that  $n_{\text{H}_2} > 10^{1.5} \text{ cm}^{-3}$  is not allowed, excluding all of the well-fitting models discussed above. In general, low  $\chi^2$  models with low densities that meet the  $K_{\text{vir}} > 0.1$  criterion under-predict the CO(3–2)/CO(1–0) line ratio by  $\gtrsim 1\sigma_{3.1}$ . Velocity gradients larger than the global value would allow the higher densities of our best-fit LVG models to satisfy the virialization requirement. In order to allow densities as high as  $10^4 \text{ cm}^{-3}$  ( $10^5 \text{ cm}^{-3}$ ) with  $K_{\text{vir}} > 0.1$ , the velocity gradient would need to be  $> 0.27 \text{ km s}^{-1} \text{ pc}^{-1}$  ( $> 0.86 \text{ km s}^{-1} \text{ pc}^{-1}$ .) If the individual clouds are virialized ( $K_{\text{vir}} = 1$ ), these  $\text{H}_2$  densities require velocity gradients of  $\sim 3 \text{ km s}^{-1} \text{ pc}^{-1}$  ( $\sim 9 \text{ km s}^{-1} \text{ pc}^{-1}$ ).

Models with low  $n_{\text{H}_2}$  and high  $N_{\text{CO}}/\Delta v$  can be elimi-

nated by requiring the CO column length to be less than the maximum source size. However, this prior requires the assumption of an upper limit for  $[\text{CO}/\text{H}_2]$ . Conservative limits (i.e.,  $[\text{CO}/\text{H}_2] < 5 \times 10^{-4}$ ; Ward et al. 2003) exclude clouds with densities comparable to or less than that seen in the Milky Way ( $\sim 10^2 \text{ cm}^{-3}$ ) along the low- $\chi^2$  degeneracy valley in the  $n_{\text{H}_2}$ - $N_{\text{CO}}/\Delta v$  plane. While this prior is not useful for distinguishing among the best-fit models for J14011, it does support the higher  $\text{H}_2$  densities preferred by the LVG analysis.

While it is unlikely that a simple LVG model will accurately capture the full range of temperatures and densities that exist in real molecular clouds, considering the degeneracies discussed above, we conclude that the bulk of the molecular gas likely has, on average,  $T_{\text{kin}} = 20$ –60 K,  $n_{\text{H}_2} \sim 10^4$ – $10^5 \text{ cm}^{-3}$ , and  $N_{\text{CO}}/\Delta v = 10^{17.00 \pm 0.25} \text{ cm}^{-2} \text{ km}^{-1} \text{ s}$ . The maximum likelihood for the thermal pressure peaks at  $\sim 10^2 \text{ K cm}^{-3}$ , but has a significant tail up to  $10^6 \text{ K cm}^{-3}$ . Measurements of other mid- $J$  CO lines, like CO(5–4), would help to better constrain these models. Using our best estimates for the LVG model parameters, we constrain  $[\text{CO}/\text{H}_2]/(\Delta v/\Delta r) = 10^{-6.7}$ – $10^{-5.2} \text{ pc km}^{-1} \text{ s}$ , which is close to the standard assumption of  $10^{-5} \text{ pc km}^{-1} \text{ s}$  used in other LVG analyses. While the measured line ratios in J14011 appear consistent with a single phase molecular ISM, analysis of other SMGs (e.g., Harris et al. 2010; Ivison et al. 2011; Danielson et al. 2011; Bothwell et al. 2012) and observations of local galaxies (e.g., Yao et al. 2003) indicate that gas in star-forming galaxies is multi-phase; i.e., it is unlikely that the gas responsible for the bulk of the CO(1–0) emission is the same gas that is emitting the CO(7–6) line, which is effectively what we are requiring by considering only single-phase models. With only three measured lines, the results of a multi-phase LVG analysis would be far too degenerate to draw meaningful conclusions about the state of molecular gas. Higher resolution observations would be helpful in establishing whether the CO lines are or are not being emitted from the same physical volumes of gas. Based on the agreement of the global line profiles for the existing CO measurements it is unlikely that excitation differences exist on large scales across J14011, but local variations with broadly similar kinematics could exist on scales below our current resolution limit.

Based on the CO abundance per unit velocity gradient of the best-fit LVG models, we can determine the CO-to- $\text{H}_2$  abundance for an assumed velocity gradient. Using the global velocity gradient from our measured line width and the Smail et al. (2005) source size, we estimate the CO-to- $\text{H}_2$  abundance to be  $[\text{CO}/\text{H}_2] = 10^{-8.6}$ – $10^{-7.1}$ , which is very low. Alternatively, if we assume more standard values of  $[\text{CO}/\text{H}_2] = 10^{-5}$ – $10^{-4}$ , the best-fit model densities return higher velocity gradients of  $\sim 1$ – $30 \text{ km s}^{-1} \text{ pc}^{-1}$ , a range that includes the necessary gradients for our best-fit models to meet the virialization criteria.

Since LVG modeling produces reasonable physical conditions for J14011, and it is only the introduction of the global velocity gradient that produces very low CO-to- $\text{H}_2$  abundance and unphysical virialization parameters, we conclude that J14011 likely has large local velocity gradients. Higher velocity gradients are possible if J14011

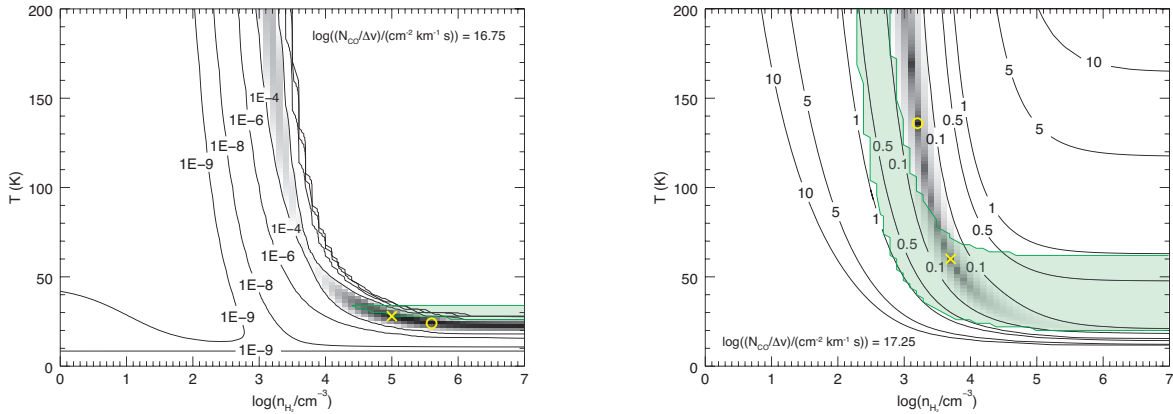


FIG. 6.— Contours of constant probability (left) and  $\chi^2$  (right) in the temperature-density plane for the best-fit values of  $N_{\text{CO}}/\Delta v$ . Models with higher probability than the highest contour (or lower  $\chi^2$  than the lowest contour) have been logarithmically shaded in greyscale. Models with parameters outside of the green-shaded region produce optically thin emission in at least one line. The best-fit models with and without the optical depth cut have been marked with yellow crosses and circles respectively.

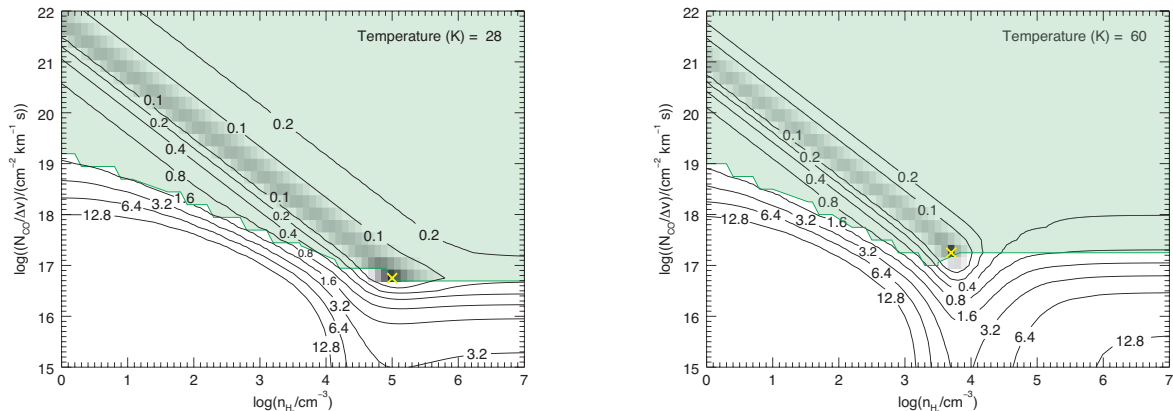


FIG. 7.— Contours of constant  $\chi^2$  in the  $n_{\text{H}_2}$ – $N_{\text{CO}}/\Delta v$  plane for highest probability optically thick model (28 K; left) and minimum  $\chi^2$  optically thick model (60 K; right). Models with  $\chi^2 < 0.1$  have been logarithmically shaded in greyscale. Models with parameters that fall below the green-shaded region produce optically thin emission. The highest probability/minimum  $\chi^2$  models in each plane are marked by the yellow crosses.

has a face-on orientation and contains numerous small clouds below our resolution limit that have turbulent velocities and/or bulk motions summing to the measured  $\text{FWHM}_{1-0} \approx 150 \text{ km s}^{-1}$ . If the individual clouds are virialized, their velocity gradients are large enough to produce more reasonable values of the CO-to- $\text{H}_2$  abundance for our best-fit densities. Although such velocity gradients would cause J14011’s molecular clouds to fall above the Galactic line-width vs. size relation (Larson 1981), such behavior has been seen in another  $z \sim 2$  SMG, SMM J2135-0102, which has a mean internal velocity gradient of  $\sim 0.5 \text{ km s}^{-1} \text{ pc}^{-1}$  for individual clumps (Swinbank et al. 2011). Swinbank et al. (2011) also find similarly high densities, and thus infer large velocity gradients under the assumption of virialization, for the molecular gas in SMM J2135-0102.

#### 4.2. Resolved star formation law

Using the aligned  $\text{H}\alpha$  and CO(1–0) maps, we plot a spatially resolved Schmidt-Kennicutt relation (Schmidt 1959; Kennicutt 1998) for J14011 in Fig. 8. We have smoothed the integrated line maps to the same spatial resolution ( $0.''70 \times 0.''65$ ), resampled to the pixel size from the SINFONI data ( $0.''25$ ), and excluded pixels that do not have at least  $2\sigma$  significance in both maps. In

order to convert the  $\text{H}\alpha$  surface luminosity to a star formation rate surface density, we use the  $L_{\text{H}\alpha}$ -SFR conversion factor given in Kennicutt (1998) scaled to match the Calzetti et al. (2007) initial mass function (IMF) used in Bigiel et al. (2008, 2010). We have also applied an additional correction to reflect the fact that the observed  $\text{H}\alpha$  luminosity underestimates the galaxy’s total star formation rate: based on the Kennicutt (1998) calibration rescaled to the Calzetti et al. (2007) IMF, J14011’s total FIR-determined SFR is  $400 M_{\odot} \text{ yr}^{-1}$ , exceeding its  $\text{H}\alpha$ -determined SFR by a factor of fifteen. Given that J14011 does not contain a strong AGN (Rigby et al. 2008), that there is good agreement between the CO and the  $\text{H}\alpha$  morphologies (unlikely if the FIR vs.  $\text{H}\alpha$  discrepancy were determined by *large-scale* patchiness in obscuration), and that the correction for the Balmer decrement as in Tecza et al. (2004) would already account for a factor of 1.5 (of the factor of 15 difference), we have simply scaled the  $\text{H}\alpha$  surface brightness of each pixel by the *global* ratio  $\text{SFR}_{\text{FIR}}/\text{SFR}_{\text{H}\alpha}$  before plotting in Fig. 8.

Converting CO(1–0) luminosity to molecular gas mass requires the assumption of a conversion factor  $\alpha_{\text{CO}}$ . Based on the results of our LVG analysis above, which produces more self-consistent molecular gas properties if the molecular ISM in J14011 is composed of mul-

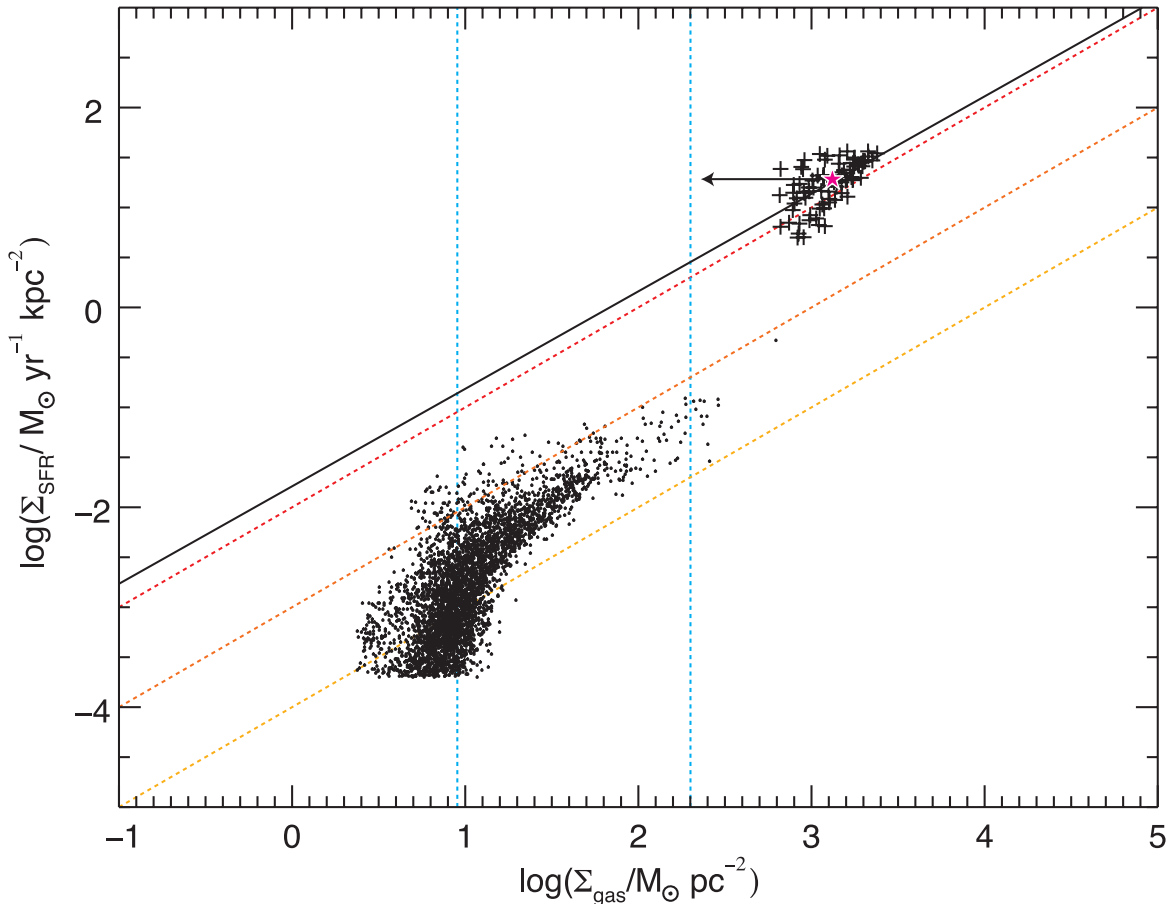


FIG. 8.— Star formation rate surface density as measured by  $H\alpha$  surface brightness (rescaled by the global  $SFR_{FIR}/SFR_{H\alpha}$ ) vs. molecular gas mass surface density for J14011 (crosses) and total gas mass surface density for local disk galaxies from Bigiel et al. (2010) (dots; clipped at  $2 \times 10^{-4} M_{\odot} \text{ yr}^{-1} \text{ kpc}^{-2}$ ). The average value for J14011 is given by the star, and a power law fit to the resolved surface density points is given by the solid line. The arrow pointing to the left shows where J14011’s locus of points (centered at the average value) would move if the molecular gas mass were calculated using the “starburst” value of  $\alpha_{CO}$  instead of the “disk” value. Dotted lines are the same as in Bigiel et al. (2008), where the diagonal lines represent the constant star formation efficiencies required to consume 1% (yellow), 10% (orange), and 100% (red) of the gas in  $10^8$  years, the left vertical line shows the HI surface density saturation, and the right vertical line marks the proposed transition between star formation laws at  $200 M_{\odot} \text{ pc}^{-2}$ .

tiple unresolved clouds rather than a single large gas reservoir, we use a fiducial Milky Way disk value of  $\alpha_{CO} = 4.6 M_{\odot} (\text{K km s}^{-1} \text{ pc}^2)^{-1}$  (Solomon & Barrett 1991). This choice is consistent with the proposed continuous form of  $\alpha_{CO}$  of Narayanan et al. (2012) for the measured metallicity of component J1 from Tecza et al. (2004) of  $12 + \log(\text{O}/\text{H}) = 8.96_{-0.10}^{+0.06}$ . In Fig. 8, the gas mass surface densities for both J14011 and the low-redshift galaxies have been scaled to account for helium. Since gravitational lensing conserves surface brightness, magnification corrections are to first order unnecessary for evaluating the resolved Schmidt-Kennicutt relation for J14011.

The resolved star formation law for J14011, as probed by the FIR-corrected  $H\alpha$  map, is not consistent with that of the local disk galaxies from Bigiel et al. (2008) despite our use of a Milky Way gas mass conversion factor. While Bigiel et al. (2008) use a sub-Milky Way value of  $\alpha_{CO} = 3.2 M_{\odot} (\text{K km s}^{-1} \text{ pc}^2)^{-1}$ , any value of  $\alpha_{CO} < 4.6$  moves J14011 further above the local relation, and  $\alpha_{CO} = 0.8$  moves it far above. Our result supports the conclusions of Genzel et al. (2010), indicating that SMGs’ position above the local star formation relation is not simply due

to the choice of CO-to- $H_2$  conversion factor. Correcting for different IMFs while respecting the differing choices in  $\alpha_{CO}$ , the star formation law for J14011 is consistent with both the SMGs in Genzel et al. (2010) (who use  $\alpha_{CO} = 1.0$ ) and the local starbursts from Kennicutt (1998) (who uses  $\alpha_{CO} = 0.8$ ), and is not consistent with the high- $z$  “normal” star-forming galaxies from Daddi et al. (2010) (who use  $\alpha_{CO} = 3.6$ ). Rescaling J14011 to the lower  $\alpha_{CO}$  used in Genzel et al. (2010) or Kennicutt (1998) would move J14011 far above the star formation relation for SMGs and low- $z$  starbursts, further supporting our choice of a Galactic CO-to- $H_2$  conversion factor for this system.

To allow comparisons to other work, we fit the star formation and molecular gas surface densities to a power law and formally retrieve a near-unity index of  $0.98 \pm 0.14$  (albeit with  $\chi^2 = 2.48$ ), consistent with indices measured in local spirals (Bigiel et al. 2008). Our application of the scaling factor to account for dust-obscured star formation does not affect our measured index, as appropriate if  $H\alpha$  traces the location of J14011’s star-forming regions, even if it does not capture the total SFR. We note that in our pixel-to-pixel comparison, the data points are not all independent due to our oversampling of the beam/point



spread function; the points in Fig. 8 are drawn from a total area of  $\sim 10$  resolution elements.

## 5. CONCLUSIONS

We present high-resolution CO(1–0) mapping of the submillimeter galaxy SMM J14011+0252. Based on a spectrally-resolved detection, we find a revised near-unity value for the CO(3–2)/CO(1–0) line ratio ( $r_{3,1} = 0.97 \pm 0.16$ ). Although  $r_{3,1}$  is closer to the average value seen in quasar-host galaxies than in SMGs, given that similar values are seen in some low- $z$  ULIRGs that lack AGN,  $r_{3,1} \sim 1$  is not inconsistent with previous observational limits on the AGN strength in J14011. J14011 may be experiencing a short period of highly-concentrated star formation affecting the gas excitation (e.g., Yao et al. 2003; Iono et al. 2009), indicating that  $r_{3,1} \sim 1$  is not a perfect discriminant between starbursts and quasar host galaxies at high redshift. We find that the position of the CO(1–0) emission agrees with those of previously detected mid- $J$  lines (Downes & Solomon 2003). The CO(1–0) emission is spatially extended from the southeast to northwest, extending between the J1s and J1n components previously identified at optical wavelengths, and showing two peaks that are slightly offset in velocity. A face-on interpretation is favored by our LVG models and is consistent with J14011’s narrow line width.

Although the results of the LVG modeling are highly degenerate and we are restricted to a single-phase analysis, our determination of the gas kinetic temperature is consistent with the gas temperature measured using C I (Walter et al. 2011) and with the dust temperature (Wu et al. 2009). Our best-fit models give  $n_{\text{H}_2} \sim 10^4\text{--}10^5 \text{ cm}^{-3}$  and  $N_{\text{CO}}/\Delta v = 10^{17.00 \pm 0.25} \text{ cm}^{-2} \text{ km}^{-1} \text{ s}$ . These densities only produce reasonable [CO/H<sub>2</sub>] values and satisfy dynamical constraints if the velocity gradi-

ent is larger than the galaxy wide-average, implying that J14011’s molecular ISM comprises numerous unresolved molecular clouds.

Based on the agreement between the metallicity-dependent version of the CO-to-H<sub>2</sub> conversion factor from Narayanan et al. (2012) and the canonical “disk” value favored by our LVG analysis, we use  $\alpha_{\text{CO}} = 4.6 M_{\odot} (\text{K km s}^{-1} \text{ pc}^2)^{-1}$  to derive a molecular gas mass of  $(1.9 \pm 0.3) \times 10^{11} M_{\odot}$  (corrected for  $\mu = 3.5$ ; Smail et al. 2005). Using H $\alpha$  data from Tecza et al. (2004), corrected by the SFR measured in the FIR, we are able to compare the spatially-resolved Schmidt-Kennicutt relation in J14011 to those of other galaxies. We find that J14011 falls above the star formation rate vs. molecular gas surface density relation seen in normal star-forming galaxies (e.g., Bigiel et al. 2008), even when we use the local “disk” value of the CO-to-H<sub>2</sub> conversion factor. This result indicates that the observed offset of starburst galaxies from the local universe Schmidt-Kennicutt law is not solely due to the use of two different gas mass conversion factors, in agreement with Genzel et al. (2010). J14011 is consistent in its star formation relation with other SMGs and starbursts when we respect different authors’ choices of gas mass conversion factor. The near-unity index of the power law fit to J14011’s points is comparable to indices measured in the local universe.

We thank an anonymous referee for helpful comments. We also thank Rob Ivison for his help obtaining the CO(1–0) observations and for useful comments, Claire Chandler for sharing insights on calibration, Ric Davies for providing the H $\alpha$  channel maps, and Dennis Downes for sharing the CO(3–2) and CO(7–6) data. This work has been supported by NSF grant AST-0708653 and NASA grant HST-GO-11143.01-A. CES has received support from an AAUW American Fellowship.

## REFERENCES

- Aguirre, P. A., Baker, A. J., Menanteau, F., Lutz, D., & Tacconi, L. J. 2012, *ApJ*, submitted
- Aravena, M., Younger, J. D., Fazio, G. G., et al. 2010, *ApJ*, 719, L15
- Arimoto, N., Sofue, Y., & Tsujimoto, T. 1996, *PASJ*, 48, 275
- Barger, A. J., Cowie, L. L., Smail, I., et al. 1999, *AJ*, 117, 2656
- Bayet, E., Gerin, M., Phillips, T. G., & Contursi, A. 2004, *A&A*, 427, 45
- . 2009, *MNRAS*, 399, 264
- Bigiel, F., Leroy, A., Walter, F., et al. 2010, *AJ*, 140, 1194
- . 2008, *AJ*, 136, 2846
- Blain, A. W. 1999, *MNRAS*, 304, 669
- Blain, A. W., Smail, I., Ivison, R. J., Kneib, J.-P., & Frayer, D. T. 2002, *Phys. Rep.*, 369, 111
- Bolatto, A. D., Leroy, A. K., Rosolowsky, E., Walter, F., & Blitz, L. 2008, *ApJ*, 686, 948
- Bothwell, M. S., Smail, I., Chapman, S. C., et al. 2012, *arXiv:1205.1511*
- Calzetti, D., Kennicutt, R. C., Engelbracht, C. W., et al. 2007, *ApJ*, 666, 870
- Carilli, C. L., Cox, P., Bertoldi, F., et al. 2002, *ApJ*, 575, 145
- Carilli, C. L., Daddi, E., Riechers, D., et al. 2010, *ApJ*, 714, 1407
- Chapman, S. C., Blain, A. W., Smail, I., & Ivison, R. J. 2005, *ApJ*, 622, 772
- Conselice, C. J., Chapman, S. C., & Windhorst, R. A. 2003, *ApJ*, 596, L5
- Daddi, E., Elbaz, D., Walter, F., et al. 2010, *ApJ*, 714, L118
- Danielson, A. L. R., Swinbank, A. M., Smail, I., et al. 2011, *MNRAS*, 410, 1687
- Dannerbauer, H., Daddi, E., Riechers, D. A., et al. 2009, *ApJ*, 698, L178
- Davé, R., Finlator, K., Oppenheimer, B. D., et al. 2010, *MNRAS*, 404, 1355
- Downes, D., & Solomon, P. M. 1998, *ApJ*, 507, 615
- . 2003, *ApJ*, 582, 37
- Downes, D., Solomon, P. M., & Radford, S. J. E. 1993, *ApJ*, 414, L13
- Engel, H., Tacconi, L. J., Davies, R. I., et al. 2010, *ApJ*, 724, 233
- Fabian, A. C., Smail, I., Iwasawa, K., et al. 2000, *MNRAS*, 315, L8
- Frayer, D. T., Ivison, R. J., Scoville, N. Z., et al. 1998, *ApJ*, 506, L7
- Frayer, D. T., Reddy, N. A., Armus, L., et al. 2004, *AJ*, 127, 728
- Frayer, D. T., Ivison, R. J., Scoville, N. Z., et al. 1999, *ApJ*, 514, L13
- Garcia-Burillo, S., Guélin, M., & Cernicharo, J. 1993, *A&A*, 274, 123
- Genzel, R., Tacconi, L. J., Gracia-Carpio, J., et al. 2010, *MNRAS*, 407, 2091
- Genzel, R., Tacconi, L. J., Combes, F., et al. 2012, *ApJ*, 746, 69
- Glover, S. C. O., & Mac Low, M.-M. 2011, *MNRAS*, 412, 337
- Goldsmith, P. F. 2001, *ApJ*, 557, 736
- Greve, T. R., Ivison, R. J., & Papadopoulos, P. P. 2003, *ApJ*, 599, 839
- . 2004, *A&A*, 419, 99
- Greve, T. R., Papadopoulos, P. P., Gao, Y., & Radford, S. J. E. 2009, *ApJ*, 692, 1432
- Greve, T. R., Bertoldi, F., Smail, I., et al. 2005, *MNRAS*, 359, 1165

- Hainline, L. J., Blain, A. W., Greve, T. R., et al. 2006, *ApJ*, 650, 614
- Harris, A. I., Baker, A. J., Zonak, S. G., et al. 2010, *ApJ*, 723, 1130
- Hinz, J. L., & Rieke, G. H. 2006, *ApJ*, 646, 872
- Iono, D., Wilson, C. D., Yun, M. S., et al. 2009, *ApJ*, 695, 1537
- Israel, F. P. 1997, *A&A*, 328, 471
- Iverson, R. J., Papadopoulos, P. P., Smail, I., et al. 2011, *MNRAS*
- Iverson, R. J., Smail, I., Barger, A. J., et al. 2000, *MNRAS*, 315, 209
- Iverson, R. J., Smail, I., Frayer, D. T., Kneib, J.-P., & Blain, A. W. 2001, *ApJ*, 561, L45
- Iverson, R. J., Smail, I., Amblard, A., et al. 2012, *MNRAS*, 425, 1320
- Kennicutt, Jr., R. C. 1998, *ApJ*, 498, 541
- Kennicutt, Jr., R. C., Calzetti, D., Walter, F., et al. 2007, *ApJ*, 671, 333
- Klamer, I. J., Ekers, R. D., Sadler, E. M., et al. 2005, *ApJ*, 621, L1
- Komatsu, E., Smith, K. M., Dunkley, J., et al. 2011, *ApJS*, 192, 18
- Larson, R. B. 1981, *MNRAS*, 194, 809
- Leroy, A., Bolatto, A., Walter, F., & Blitz, L. 2006, *ApJ*, 643, 825
- Mao, R. Q., Henkel, C., Schulz, A., et al. 2000, *A&A*, 358, 433
- Mauersberger, R., Henkel, C., Walsh, W., & Schulz, A. 1999, *A&A*, 341, 256
- Meier, D. S., Turner, J. L., Beck, S. C., et al. 2010, *AJ*, 140, 1294
- Motohara, K., Takata, T., Iwamuro, F., et al. 2005, *AJ*, 129, 53
- Narayanan, D., Cox, T. J., Hayward, C. C., & Hernquist, L. 2011, *MNRAS*, 412, 287
- Narayanan, D., Hayward, C. C., Cox, T. J., et al. 2010, *MNRAS*, 401, 1613
- Narayanan, D., Krumholz, M. R., Ostriker, E. C., & Hernquist, L. 2012, *MNRAS*, 421, 3127
- Neri, R., Genzel, R., Iverson, R. J., et al. 2003, *ApJ*, 597, L113
- Nesvadba, N. P. H., Lehnert, M. D., Genzel, R., et al. 2007, *ApJ*, 657, 725
- Oka, T., Hasegawa, T., Hayashi, M., Handa, T., & Sakamoto, S. 1998, *ApJ*, 493, 730
- Papadopoulos, P., Iverson, R., Carilli, C., & Lewis, G. 2001, *Nature*, 409, 58
- Riechers, D. A., Carilli, C. L., Walter, F., & Momjian, E. 2010, *ApJ*, 724, L153
- Riechers, D. A., Walter, F., Carilli, C. L., et al. 2006, *ApJ*, 650, 604
- Riechers, D. A., Carilli, C. L., Maddalena, R. J., et al. 2011a, *ApJ*, 739, L32
- Riechers, D. A., Carilli, L. C., Walter, F., et al. 2011b, *ApJ*, 733, L11
- Rigby, J. R., Marcellac, D., Egami, E., et al. 2008, *ApJ*, 675, 262
- Schmidt, M. 1959, *ApJ*, 129, 243
- Scoville, N. Z., Sargent, A. I., Sanders, D. B., & Soifer, B. T. 1991, *ApJ*, 366, L5
- Scoville, N. Z., Yun, M. S., & Bryant, P. M. 1997, *ApJ*, 484, 702
- Serjeant, S. 2012, *MNRAS*, 424, 2429
- Smail, I., Iverson, R. J., Blain, A. W., & Kneib, J. 1998, *ApJ*, 507, L21
- . 2002, *MNRAS*, 331, 495
- Smail, I., Smith, G. P., & Iverson, R. J. 2005, *ApJ*, 631, 121
- Solomon, P. M., & Barrett, J. W. 1991, in *IAU Symposium*, Vol. 146, *Dynamics of Galaxies and Their Molecular Cloud Distributions*, ed. F. Combes & F. Casoli, 235
- Solomon, P. M., Downes, D., Radford, S. J. E., & Barrett, J. W. 1997, *ApJ*, 478, 144
- Swinbank, A. M., Smail, I., Chapman, S. C., et al. 2004, *ApJ*, 617, 64
- Swinbank, A. M., Smail, I., Longmore, S., et al. 2010, *Nature*, 464, 733
- Swinbank, A. M., Papadopoulos, P. P., Cox, P., et al. 2011, *ApJ*, 617, 11
- Tacconi, L. J., Neri, R., Chapman, S. C., et al. 2006, *ApJ*, 640, 228
- Tacconi, L. J., Genzel, R., Smail, I., et al. 2008, *ApJ*, 680, 246
- Tecza, M., Baker, A. J., Davies, R. I., et al. 2004, *ApJ*, 605, L109
- Thomson, A. P., Iverson, R. J., Smail, I., et al. 2012, *MNRAS*, 425, 2203
- Walter, F., Weiß, A., Downes, D., Decarli, R., & Henkel, C. 2011, *ApJ*, 730, 18
- Ward, J. S. 2002, PhD thesis, California Institute of Technology
- Ward, J. S., Zmuidzinas, J., Harris, A. I., & Isaak, K. G. 2003, *ApJ*, 587, 171
- Wei, L. H., Vogel, S. N., Kannappan, S. J., et al. 2010, *ApJ*, 725, L62
- Weiß, A., Downes, D., Henkel, C., & Walter, F. 2005, *A&A*, 429, L25
- Weiß, A., Downes, D., Walter, F., & Henkel, C. 2007, in *Astronomical Society of the Pacific Conference Series*, Vol. 375, *From Z-Machines to ALMA: (Sub)Millimeter Spectroscopy of Galaxies*, ed. A. J. Baker, J. Glenn, A. I. Harris, J. G. Mangum, & M. S. Yun, 25
- Wilson, C. D. 1995, *ApJ*, 448, L97
- Wu, J., Vanden Bout, P. A., Evans, II, N. J., & Dunham, M. M. 2009, *ApJ*, 707, 988
- Yao, L., Seaquist, E. R., Kuno, N., & Dunne, L. 2003, *ApJ*, 588, 771
- Zhu, M., Seaquist, E. R., & Kuno, N. 2003, *ApJ*, 588, 243